Wiley Online Library
Early View publication on www.wileyonlinelibrary.com
(issue and page numbers not yet assigned;
citable using Digital Object Identifier – **DOI**)

Phys. Status Solidi B, 1–7 (2016) / **DOI** 10.1002/pssb.201600543

physica status solidi b
www.pss-b.com
basic solid state physics

Depth sensitive X-ray diffraction as a probe of buried half-metallic inclusions

C. W. Burrows, T. P. A. Hase, M. J. Ashwin, P. J. Mousley, and G. R. Bell*

Department of Physics, University of Warwick, Coventry CV4 7AL, UK

Received 14 August 2016, revised 4 October 2016, accepted 5 October 2016
Published online 31 October 2016

Keywords epitaxy, half-metals, spintronics, X-ray diffraction

* Corresponding author: e-mail gavin.bell@warwick.ac.uk, Phone: +44-24-76523489, Fax: +44-24-76150897

The ferromagnetic material MnSb can exist in two polymorphs in epitaxial thin-film form, namely niccolite n-MnSb and cubic c-MnSb. We investigate the behavior of these polymorphs using grazing incidence depth-dependent in-plane X-ray diffraction. The in-plane lattice parameter evolution of a nominal 3000 Å thin film reveals a small near-surface compression of ∼0.1% in the majority n-MnSb component. A similar effect is also observed for the cubic polymorph, suggesting that the local strain environment of these crystallites is dominated by the n-MnSb matrix.

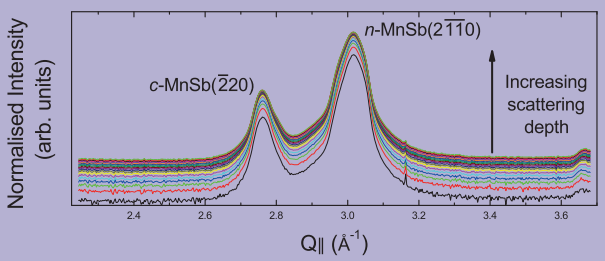

Collated in-plane X-ray diffraction data from a GaAs/$In_{0.5}Ga_{0.5}As$(111)/MnSb heterostructure in the near-surface region with probing depths ranging between 20 and 450 Å. Present are two of the polymorphs of MnSb: the niccolite (n-) and cubic zincblende (c-) phases.

1 Introduction Half-metallic ferromagnetic (HMF) materials have high potential in hybrid semiconductor spintronic devices, especially if they can be grown in thin films. Molecular beam epitaxy (MBE) has been used to grow a variety of thin-film HMF materials including semi-Heusler alloys [1, 2], full-Heusler alloys [3–5], and binary transition-metal pnictides including MnSb [6–10]. Of the HMF family of materials, the binary transition-metal pnictides, in particular those containing Mn, are especially attractive candidates for thin film spintronic applications due to their epitaxial and chemical compatibility with a range of semiconducting substrates. The Mn pnictides are not HMF materials in their usual niccolite hexagonal (n-) polymorph. However, zincblende cubic (c-) polymorphs of MnBi [11], MnSb [12], and MnAs [13] are predicted to be HMF materials. Furthermore, according to extended density functional theory calculations incorporating finite temperature effects through the disordered local moments approach, c-MnSb promises a wide minority spin gap and robust 100% spin polarization even at room temperature [12].

There exist several demonstrated "hybrid material" device applications featuring the combination of MnSb [14–16] and MnAs [17–19] with semiconducting layers. To fully realize the potential of such hybrid spintronic materials requires improvements in the spin polarization at room temperature. One possible route to achieving this aim is to exploit the highly spin-polarized c-MnSb (or c-MnAs) polymorph. We have shown that c-MnSb crystallites can coexist in MBE-grown n-MnSb epilayers [12, 20] grown on III–V compound semiconductors and it is plausible that the inclusion of this HMF polymorph could improve the magnetic properties of these layers if a detailed spatially resolved structural characterization of the polymorphic components can be determined in such MBE-grown MnSb epilayers.

The bulk structure of n-MnSb is the double hexagonal close packed $B8_1$ structure with lattice parameters $a = 4.128$ Å and $c = 5.789$ Å [21]. Conversely, c-MnSb has the cubic B3 zincblende structure and we have observed lattice parameters b of between 6.435 and 6.502 Å [12, 20] (in this paper, cubic materials are assigned lattice parameters b_i). The somewhat large range of observed cubic lattice parameters is due to their strong correlation with inclusion crystallite size. The epitaxial mismatch between the majority n-MnSb layer and the $In_{0.5}Ga_{0.5}As(111)A$ virtual substrate is only ∼0.31%. However, a far larger mismatch of 10.1% exists between the n-MnSb matrix and the c-MnSb polymorph embedded within it. It is this very high mismatch which causes the variation in c-MnSb lattice parameter with crystallite size.

In the present paper, we make use of the high fluxes and increased angular resolution available at synchrotron radiation sources to explore the depth-dependent behavior of MnSb epilayers grown on $In_{0.5}Ga_{0.5}As(111)A$ substrates. We use grazing incidence in-plane X-ray diffraction (GIXRD) to determine the crystallographic behavior of the near-surface region of a nominally 3000 Å thick MnSb(0001) film.

2 Experimental details A 3000 Å thick MnSb epilayer was grown on an $In_{0.5}Ga_{0.5}As(111)A$ virtual substrate by MBE using optimized growth conditions [20]. The sample was not capped with Sb, which we typically use to passivate the surface and prevent oxidation [22], in order to avoid confusion between diffraction features arising from the cubic polymorph and elemental Sb.

High-resolution XRD experiments were performed using 10 keV photons at the ESRF synchrotron (France) on the XMaS beamline. The diffractometer was operated in a six-circle configuration and the experiments were performed at atmospheric pressure with the sample under flowing nitrogen. The sample rested on two additional perpendicular arcs of rotation to ensure that the surface was flat with respect to the incident X-ray beam within an error of less than 0.05°. For the symmetric out-of-plane experiments (where Q is aligned parallel to the surface normal), the system was operated in a pseudo four-circle mode with standard coupled θ_V-$2\theta_V$ scans performed alongside asymmetric reciprocal space maps. Further details are given in Ref. [20]. For the in-plane symmetric scans (where Q is perpendicular to the surface normal), a series of azimuthal sample rotations coupled with in-plane arm movement θ_H–$2\theta_H$ was used as a function of sample azimuth. A schematic of the diffraction geometry used is given in Fig. 1. For depth dependence studies, a small incident angle α_i was induced by tilting the entire diffractometer about its center of rotation. This ensured the incident angle remained fixed as a function of sample rotation. The optimized α_f was found by maximizing the scattered intensity by scanning $2\theta_V$.

3 Scattering geometry When the incidence angle of the primary X-ray beam is below the value for the critical angle then total external reflection occurs and only an evanescent wave penetrates into the sample surface. As a consequence, the effective penetration depth of the X-ray beam drops dramatically, typically down to tens of Å. This results in a high level of surface specificity which can be controlled through adjustment of incident angle [23]. We note that an advantage of the in-plane geometry used here for depth-dependent studies is that refractive effects are minimized and so Q remains unchanged, unlike other depth-sensitive scattering techniques such as parallel beam powder diffraction, to determine the effective scattering depth, defined as the depth at which the electric field has been reduced by a value of $1/e$, as a function of incident angle we use the formalism developed by Dosch et al. [24]. The scattering depth Λ is given by

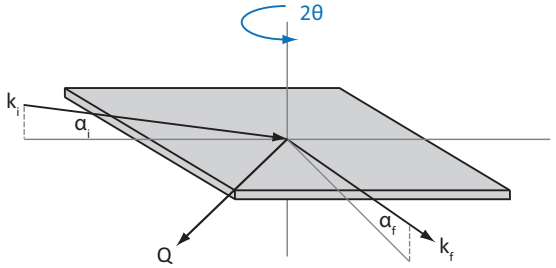

Figure 1 Schematic of the in-plane diffraction geometry used, $\mathbf{k}_i$ and $\mathbf{k}_f$ are the incident and final X-ray wave-vectors, $\mathbf{Q}$ is the scattering vector, which is very nearly in-plane and features a small Q_z component. α_i and α_f are incident and final grazing angles.

$$\Lambda = \frac{\lambda}{2\pi(l_i + l_f)}, \tag{1}$$

where l_i and l_f are

$$l_{i,f} = \frac{\sqrt{2}}{2}\{(2\delta - \sin^2\alpha_{i,f})^2 + [(\sin^2\alpha_{i,f} - 2\delta)^2 + (2\beta)^2]^{\frac{1}{2}}\}^{\frac{1}{2}}. \tag{2}$$

Here, δ and β relate to dispersion and absorption effects in the complex refractive index of the near surface region. The angles $\alpha_{i,f}$ are the angles of the primary (incident) and scattered (final) X-ray beams with respect to the sample surface defined in Fig. 1. For MnSb at 10 keV, the values of δ and β are 1.227×10^{-5} and 9.47×10^{-7}, respectively. The variation in scattering depth calculated from Eq. (1) as a function of incident angle is shown in Fig. 2. Due to the presence of a non-stoichiometric surface oxide [25], the use of values for δ and β derived for pure MnSb may introduce a small systematic error on the calculated scattering depth. The penetration depth varies from approximately 20 Å at very low angles to ∼750 Å for an incident angle of 0.5°. However, scattering will be measured from a depth up to three times greater than these values due to the slowly decaying amplitude of the electric field into the sample. The dashed line in the main figure body highlights the position of the critical angle, α_c, at 0.284° as calculated using the relation $\alpha_c = \lambda \cdot (r_e \cdot \rho_{e^-}/\pi)^{\frac{1}{2}}$. Above this angle, total external reflection no longer occurs and the scattering volume increases rapidly. The inset in Fig. 2 shows the behavior of the scattering depth for incidence angles

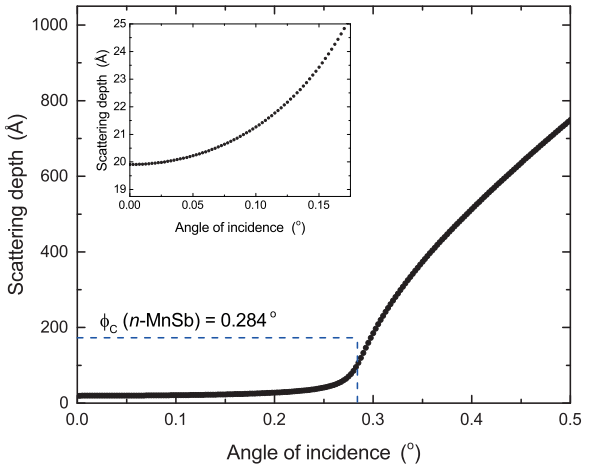

Figure 2 The scattering depth Λ calculated for n-MnSb. The inset shows low angles, well below the critical angle ϕ_c for n-MnSb, at an expanded scale.

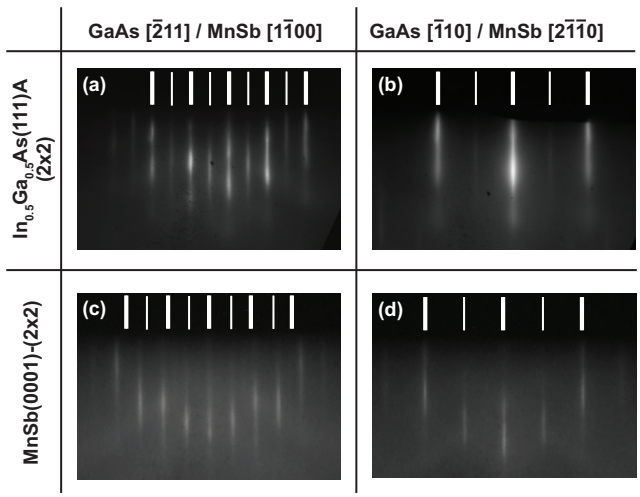

Figure 3 Typical RHEED patterns before and after MnSb growth on the $In_{0.5}Ga_{0.5}As(111)A$ virtual substrate.

between 0 and 0.17° showing the depth sensitivity of the technique at very grazing angles.

4 Results and discussion Figure 3 shows RHEED patterns obtained from the clean $In_{0.5}Ga_{0.5}As(111)A$ virtual substrate and the MnSb(0001) layer after growth. The patterns exhibit the expected (2 × 2) reconstruction for both surfaces [8, 20]. The patterns confirm the in-plane epitaxial relation as GaAs[$\bar{1}$10] parallel to MnSb[2$\bar{1}\bar{1}$0] which is consistent with our growth on both GaAs and Ge substrates. The spacing of the RHEED streaks is consistent with an in-plane surface lattice parameter of $a = 4.14 \pm 0.05$ Å, the value usually measured for relaxed MnSb(0001). Using conventional out-of-plane symmetric XRD, the lattice parameters of the $In_{0.5}Ga_{0.5}As(111)A$ substrate and the n-MnSb film are $b_{sub} = (5.853 \pm 0.001)$ Å and $c = (5.768 \pm 0.001)$ Å, respectively. On the basis of asymmetric reciprocal space mapping, the in-plane n-MnSb lattice parameter is (4.153 ± 0.008) Å. The mosaic width of the virtual substrate (0.543°) is determined by the relatively large epitaxial mismatch between it and the GaAs substrate (∼3.7%), and this mosaicity influences the crystal quality of the MnSb epilayer. Both XRD and electron microscopy have revealed crystalline inclusions of c-MnSb within the predominantly n-MnSb film [20]. The in-plane and out-of-plane lattice parameters of these cubic inclusions are (6.429 ± 0.008) Å and (6.435 ± 0.008) Å, respectively.

In-plane GIXRD data with Q aligned along both principal in-plane directions were obtained using the geometry shown in Fig. 1 and all data sets were fitted carefully using a reduced χ^2 minimization routine. Peaks were fitted using Pearson VII functions and backgrounds were fitted with either polynomials (long Q range scans) or tanh functions (short Q range scans). Care was taken to avoid artefacts due to background choice. The uncertainties on fitting parameters were found by determining the extent of the $\Delta\chi^2 = 1$ contour [26].

Typical in-plane GIXRD data obtained at an incidence angle of 0.5° ($\Lambda = 750$ Å) are shown in Fig. 4, with Q aligned along the GaAs[$\bar{1}$10] and GaAs[$\bar{2}$11] directions along with total fits, peak components, and background (sixth order polynomial). Focusing on the GaAs[$\bar{1}$10] direction first, the expected n-MnSb{2110} and c-MnSb{220} reflections are present. To obtain a good fit, an additional but small peak was required. This additional scattering may either arise from diffuse scattering from defects or, more likely, from the $In_{0.5}Ga_{0.5}As$ substrate. The substrate peak is broadened as we are relatively far from the diffraction condition, only measuring the tails of the ($\bar{2}$20) peak convolved with the crystal truncation rod. The asymmetric shape of the n-MnSb(4$\bar{2}\bar{2}$0) and c-MnSb($\bar{2}$20) reflections suggest that they consist of two sets of reflections arising from crystallites with distinct lattice parameters. In fact, it was not possible to satisfactorily fit the data without two contributions for each of the four diffraction peaks. For c-MnSb, the dominant sub-peak in each pair (solid green lines) appears at lower Q values while for n-MnSb, the larger sub-peak appears at higher Q values (solid red lines). The data with Q aligned along the GaAs[$\bar{2}$11] direction are somewhat simpler, with only two diffraction features present (Fig. 4b), These are indexed to the c-MnSb($\bar{4}$22) and n-MnSb(3$\bar{3}$00). The fitting reveals that these sub-peaks correspond to n-MnSb lattice parameters of $a_1 = (4.152 \pm 0.001)$ Å and $a_2 = (4.188 \pm 0.001)$ Å, and c-MnSb parameters of $b_1 = (6.429 \pm 0.001)$ Å and $b_2 = (6.347 \pm 0.004)$ Å (suffix 1 denotes the more intense sub-peak in each case). Both in-plane parameters are consistent with the (less accurate) RHEED measurements.

Additional in-plane XRD scans were collected along the GaAs[$\bar{1}$10] direction over a reduced Q range, focusing on the c-MnSb($\bar{2}$20) and n-MnSb(2$\bar{1}\bar{1}$0) reflections, with increased point density. The angle of incidence was varied between 0.025° and 0.375° in 0.025° steps so that the scattering depth changed between 20 and 450 Å. As with the larger Q-range scans two sub-peaks for each of the c-MnSb and n-MnSb

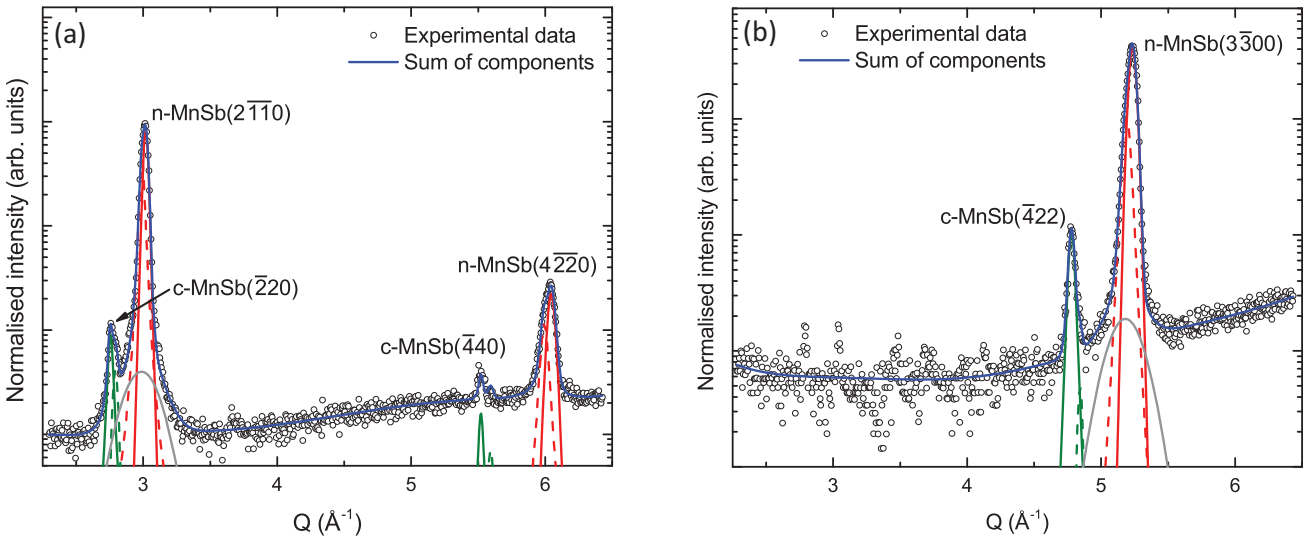

Figure 4 In-plane GIXRD scans with Q aligned along the (a) GaAs[$\bar{1}$10] direction and (b) GaAs[$\bar{2}$11] direction. Along both directions, four diffraction peaks due to c-MnSb (green) and n-MnSb (red) are labeled, the solid lines indicate the most intense component. The gray lines correspond to weak reflections from the $In_{0.5}Ga_{0.5}As$(111)A/GaAs(111)A virtual substrate.

were used, with a low intensity $In_{0.5}Ga_{0.5}As$(111)A reflection included at the expected ($\bar{2}$20) position. For scattering depths below 70 Å, the c-MnSb b_2 lattice parameter was constrained to values smaller than 6.350 Å. This was done such that the intensity of the second cubic component could be determined without introducing fitting artefacts whereby the b_2 sub-peak would end up distorting to accommodate the tails of the a_1 sub-peak. As such, it should be noted that the area of the b_2 peak as determined from fitting is only broadly representative of the scattered intensity. Figure 5 shows a typical reduced Q range GIXRD scan, with best fit to the data, for an incidence angle of 0.375° ($\Lambda = 450$ Å). The inset of Fig. 5 shows a close-up of the n-MnSb(2$\bar{1}\bar{1}$0) reflections on a linear vertical scale, highlighting the quality of the fit to the data.

The evolution of the n-MnSb a_1 and a_2 lattice parameters is shown in Fig. 6a(i) and (ii). The n-MnSb a_1 parameter varies from (4.150 ± 0.001) Å to (4.154 ± 0.001) Å while the a_2 parameter varies between (4.183 ± 0.001) Å to (4.193 ± 0.001) Å for scattering depths of 20 and 450 Å. These represent −0.1% and −0.25% changes in a_1 and a_2, respectively, relative to the lattice parameters at high Λ. The c-MnSb lattice parameters (not shown) exhibit similar changes over the scattering depths probed although the b_2 parameter settles at a constraint value below scattering depths of 70 Å. The b_1 parameter changes from (6.417 ± 0.001) Å in the near surface region to (6.424±0.001) Å deeper into the film, a –0.1% shift. The red dashed lines in Fig. 6a(i) and (ii) are exponential functions fitted to the data to highlight the near-surface decay of the parameters. The decay constant for the a_1 parameter is (17 ± 5) Å while for a_2 it is (12 ± 3) Å. This suggests that the relaxation observed in the near-surface region extends over approximately 40 Å (including the minimum 20 Å scattering depth arising from the evanescent wave present in the sample).

The lattice parameter of bulk single-crystal MnSb is $a = 4.128$ Å, smaller than the values of a_1 and a_2 observed here. It is possible that even strain-relaxed (0001) thin-film material still contains extended defects which increase the in-plane lattice parameter from the value for bulk material. A bimodal lattice parameter distribution could arise from the formation of anti-phase boundaries (APBs), which would

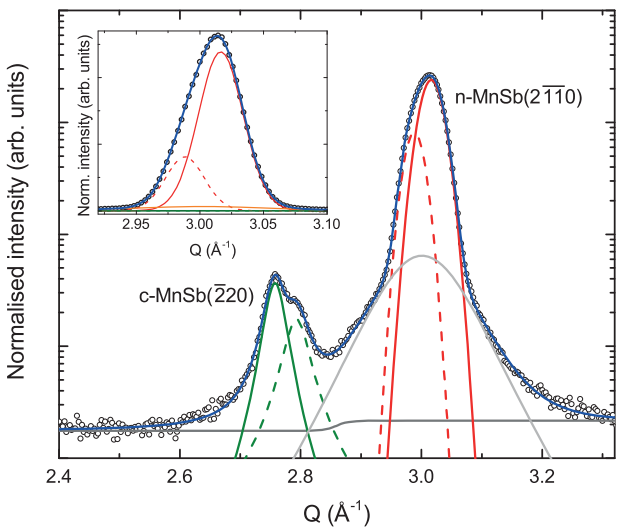

Figure 5 Typical GIXRD in-plane scan with corresponding best fit, obtained with an incidence angle of 0.375° ($\Lambda = 450$ Å). Reflections from c-MnSb (green), n-MnSb (red) and the $In_{0.5}Ga_{0.5}As$(111)A substrate (gray) are present. The inset shows a zoom of the n-MnSb(2$\bar{1}\bar{1}$0) region on a linear scale.

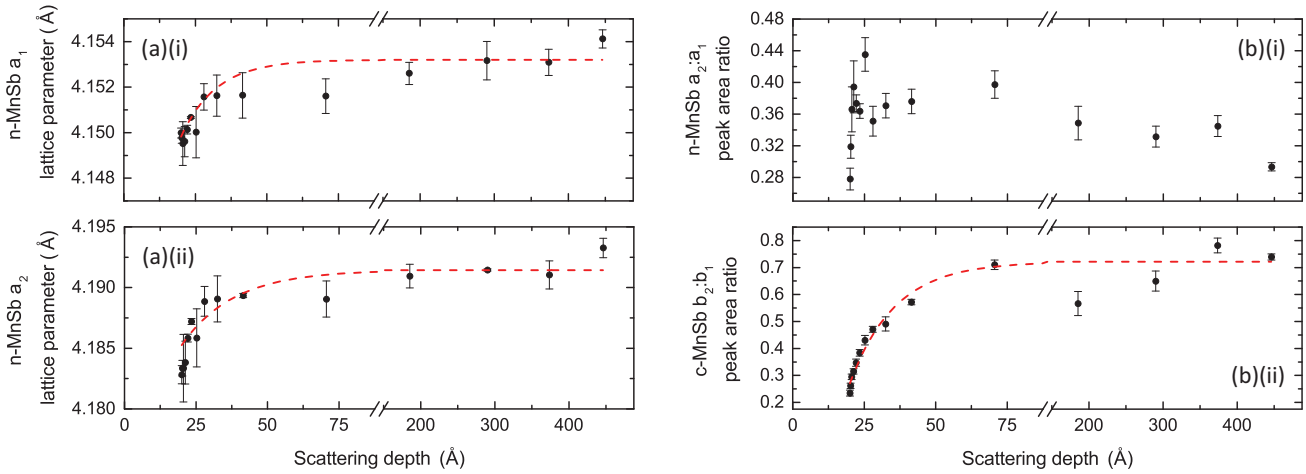

Figure 6 Evolution of the n-MnSb in-plane lattice parameters (a)(i) a_1 and (a)(ii) a_2 as a function of scattering depth. Change in peak area ratio for the (b)(i) n-MnSb and (b)(ii) c-MnSb sub-peaks as a function of scattering depth. The dashed red lines correspond to fitted exponential decay functions, which also serve as a guide to the eye.

occur in this material system due to the difference in stacking orders within the film caused by terrace steps on the substrate. The $In_{0.5}Ga_{0.5}As(111)A$ virtual substrate has surface step heights $b/\sqrt{3} = 3.38$ Å, not far from the value of $c/2 = 2.89$ Å for n-MnSb. The stacking of hexagonal close-packed planes in the n-MnSb $B8_1$ structure is ABAC, with Mn on A sites and Sb on B and C sites. It is possible that n-MnSb APBs, extending throughout the film, arise due to regions with Mn–B–Mn–C stacking adjoining regions with Mn–C–Mn–B stacking. The steric effect among Sb atoms in adjoining regions would tend to increase the in-plane lattice parameter, but this effect would be much smaller out-of-plane due to the separation of Sb layers by the intervening layers of Mn. On this basis, regions with measured lattice parameter a_2 could be those including APBs, while a_1 is representative of APB-free n-MnSb, and the c parameter would not be expected to change significantly.

The near-surface relaxation observed could arise from several effects. Relatively thick Mn-rich native oxide layers can form on uncapped MnSb films which *in extremis* can extend to ∼5 nm [25]. This amorphous oxide, which damps the electric field in the sample and thereby reducing the intensity of the observed diffraction peaks, could induce strain in the neighboring MnSb, although this effect is difficult to quantify given its non-stoichiometric composition and lack of long range crystalline order. Surface roughness and a locally variable oxide layer thickness could allow some in-plane relaxation of the MnSb at the surface. It is also possible that oxide formation is enhanced along extended defects near the surface leading to relaxation of their associated strain. This is consistent with the increased relaxation observed in the a_2 lattice parameter compared to a_1, if a_2 is attributed to defective n-MnSb.

Figure 6b(i) and (ii) show the ratio of the sub-peak areas for the n-MnSb and c-MnSb reflections, respectively. In the n-MnSb a_2 to a_1 ratio [panel (b)(i)], there is an increase from (0.278 ± 0.014) to ∼0.36 as the scattering depth decreases although no clear trend is present since the ratio returns to ∼0.28 at small scattering depths. It can be seen that both defective and non-defective MnSb are present throughout the upper 450 Å of the film. This would be consistent with APBs which are not readily "healed" during epitaxy. It is known that threading dislocations with Burgers vector $(c/2)[0001]$ penetrate to the surface of MnSb/GaAs(111) films [8], and localized misfit dislocation arrays have been observed at the interfaces [12, 20] but a more extensive study of extended defects would be required to understand in detail the behavior of this epitaxial system.

Figure 6b(ii) shows the ratio of the c-MnSb b_2 to b_1 peak areas which reveals a much clearer trend. At higher scattering depths ($\Lambda \geq 70$ Å) both components are present with similar peak area. Toward the surface the proportion of the b_2 component ($b_2 < b_1$) drops off significantly, with a similar decay length to those observed for the lattice parameter changes. On the basis of the out-of-plane measurements presented in Ref. [20], the lower Q c-MnSb component is the more prevalent in the layer with the smaller lattice parameter component existing deeper into the film. This is consistent with the present in-plane results. Even though the dominant c-MnSb component with larger b_1 becomes more prevalent near the surface, its own lattice parameter relaxes downward along with that of the surrounding n-MnSb matrix. This suggests that in-plane relaxation due to the proximity of the surface and native oxide is mediated to the c-MnSb inclusions via the n-MnSb matrix. The relaxation toward the surface observed in Fig. 6 is independent of any systematic error in the determination of the incident angle which would only cause a slight shift along the depth axis.

We can compare the lattice parameters determined from this in-plane study to those obtained in our previous paper [20]. In that work, we could derive accurate out-of-plane lattice parameters averaged over the whole film thickness (via standard symmetric diffraction) but only approximate in-plane parameters (via asymmetric reciprocal space maps

– RSMs). The limited Q resolution of the RSMs precludes a detailed determination of the lattice parameters from such data. From the RSM peak maxima, however, we can estimate the in-plane lattice parameters of the dominant phases. These are in excellent agreement with the a_1 and b_1 values reported herein. Symmetric scans recorded along the n-MnSb [0001] direction with higher Q resolution showed a two-component peak at the c-MnSb(111) position (Figs. 3(b) and 4(b) of [20]). The lattice parameters of these components are in agreement with both b_1 and b_2, consistent with undistorted cubic structures. Conversely, no such split into two components is observed at the n-MnSb(0002) peak position. This is consistent with the presence of APBs extending throughout the thickness of the film which affect the a parameter much more strongly than the c parameter.

5 Conclusion We have exploited the tunable depth sensitivity of GIXRD when performed on a six-circle diffractometer to study in-plane diffraction from a MnSb (0001) thin film grown on an $In_{0.5}Ga_{0.5}As$(111)A virtual substrate. The predominantly n-MnSb epilayer contains strained c-MnSb(111) crystallites which extend at least 400 Å into the film. For both polymorphs, the in-plane XRD must be fitted with two components of slightly different lattice parameters. For the n-MnSb polymorph, it is suggested that extended defects such as APBs are responsible for the component with larger lattice parameter. For c-MnSb, the stronger in-plane lattice parameter [(6.429 ± 0.001) Å] is in excellent agreement with lattice parameters [(6.429 ± 0.008) Å] for thin films on $In_{0.5}Ga_{0.5}As$(111)A measured previously by reciprocal space mapping [20]. All of the lattice parameters vary with depth, with both n-MnSb values relaxing to lower values within $\sim$ 40 Å of the surface. The stronger c-MnSb peak follows this relaxation while the weaker component at smaller lattice parameter drops in intensity toward the surface.

This work confirms that c-MnSb inclusions can be stabilized within n-MnSb epilayers and shows additionally that the strain state of the c-MnSb is linked to that of the surrounding n-MnSb matrix. Our density functional theory (DFT) work suggests that over the range of strains observed in c-MnSb the material remains robustly HMF, important for its application in spintronics. Further, DFT work would be valuable in assessing the local role of strain and extended defects such as APBs on the magnetic properties of both n-MnSb and c-MnSb.

The GIXRD method can provide detailed depth-resolved information on varying strain states within an epitaxial film as close as 20 Å to the surface without the need for ultra-high vacuum. Even for the low-strain films studied here, significant surface relaxation has been observed. We will discuss results on Sb-capped ultra-thin (10 Å to 50 Å) MnSb(0001)/GaAs(111) films in a future paper, where the in-plane strain due to epitaxial mismatch with the substrate is dominant.

Acknowledgements This work was supported by EPSRC (UK) under grant numbers EP/K032852/1 and EP/K03278X/1. XMaS is a mid-range facility funded by EPSRC. We are grateful to the beamline staff at XMaS and to R. Johnston at Warwick for their expert help and technical assistance.

References

[1] W. V. Roy, J. D. Boeck, B. Brijs, and G. Borghs, Appl. Phys. Lett. 77(25), 4190–4192 (2000).
[2] P. Bach, A. S. Bader, C. Ruster, C. Gould, C. R. Becker, G. Schmidt, L. W. Molenkamp, W. Weigand, C. Kumpf, E. Umbach, R. Urban, G. Woltersdorf, and B. Heinrich, Appl. Phys. Lett. **83**(3), 521–523 (2003).
[3] B. Kuerbanjiang, Z. Nedelkoski, D. Kepaptsoglou, A. Ghasemi, S. E. Glover, S. Yamada, T. Saerbeck, Q. M. Ramasse, P. J. Hasnip, T. P. A. Hase, G. R. Bell, K. Hamaya, A. Hirohata, and V. K. Lazarov, Appl. Phys. Lett. **108**, 172412 (2016); http://dx.doi.org/10.1063/1.4948466.
[4] M. Kawano, S. Yamada, S. Oki, K. Tanikawa, M. Miyao, and K. Hamaya, Jpn. J. Appl. Phys. **52**(4S), 04CM06 (2013).
[5] S. Yamada, K. Tanikawa, S. Oki, M. Kawano, M. Miyao, and K. Hamaya, Appl. Phys. Lett. **105**, 071601 (2014)
[6] S. Liu, S. M. Bedair, and N. A. El-Masry, Mater. Lett. **42**(1–2), 121–129 (2000).
[7] H. Tatsuoka, H. Kuwabara, M. Oshita, T. Nakamura, H. Fujiyasu, and Y. Nakanishi, Thin Solid Films **281–282**, 499–502 (1996).
[8] S. Hatfield and G. R. Bell, Surf. Sci. **601**(23), 5368–5377 (2007).
[9] J. D. Aldous, C. W. Burrows, I. Maskery, M. Brewer, D. Pickup, M. Walker, J. Mudd, T. P. A. Hase, J. A. Duffy, S. Wilkins, C. Sánchez-Hanke, and G. R. Bell, J. Cryst. Growth **357**, 1–8 (2012).
[10] C. W. Burrows, A. Dobbie, M. Myronov, T. P. A. Hase, S. B. Wilkins, M. Walker, J. J. Mudd, I. Maskery, M. R. Lees, C. F. McConville, D. R. Leadley, and G. R. Bell, Cryst. Growth Des. **13**(11), 4923–4929 (2013).
[11] Y. Q. Xu, B. G. Liu, and D. G. Pettifor, Physica B **329**, 1117 (2002).
[12] J. D. Aldous, C. W. Burrows, A. M. Sánchez, R. Beanland, I. Maskery, M. K. Bradley, M. dos Santos Dias, J. B. Staunton, and G. R. Bell, Phys. Rev. B **85**, 060403(R) (2012).
[13] S. D. Guo and B. G. Liu, EPL **93**, 47006 (2011).
[14] T. Hanna, D. Yoshida, and H. Munekata, J. Cryst. Growth **323**(1), 383–386 (2011).
[15] W. Terui, H. Munekata, T. Hanna, and D. Yoshida, Phys. Status Solidi C **8**(2), 396–398 (2011).
[16] T. Amemiya, Y. Ogawa, H. Shimizu, H. Munekata, and Y. Nakano, Appl. Phys. Express **1**(2), 022002 (2008).
[17] H. Kum, S. Jahangir, D. Basu, D. Saha, and P. Bhattacharya, Appl. Phys. Lett. **99**, 152503 (2011).
[18] E. D. Fraser, S. Hegde, L. Schweidenback, A. H. Russ, A. Petrou, H. Luo, and G. Kioseoglou, Appl. Phys. Lett. **97**, 041103 (2010).
[19] D. Basu, D. Saha, C. C. Wu, M. Holub, Z. Mi, and P. Bhattacharya, Appl. Phys. Lett. **92**, 091119 (2008).
[20] G. R. Bell, C. W. Burrows, T. P. A. Hase, M. J. Ashwin, S. R. C. McMitchell, A. M. Sanchez, and J. D. Aldous, SPIN **04**, 1440025 (2014).
[21] B. T. M. Willis and H. P. Rooksby, Proc. Phys. Soc. B **67**(4), 290 (1954).
[22] J. D. Aldous, C. W. Burrows, I. Maskery, M. S. Brewer, T. P. A. Hase, J. A. Duffy, M. R. Lees, C. Sánchez-Hanke,

T. Decoster, W. Theis, A. Quesada, A. K. Schmid, and G. R. Bell, J. Phys.: Condens. Matter **14**, 146002 (2012).
[23] B. K. Tanner, T. P. A. Hase, T. A. Lafford, and M. S. Goorsky, Adv. X-Ray Anal. **47**, 309 (2003).
[24] H. Dosch, B. W. Batterman, and D. C. Wack, Phys. Rev. Lett. **56**(11), 1144–1147 (1986).
[25] S. Hatfield, J. Aldous, and G. R. Bell, Appl. Surf. Sci. **255**(6), 3567–3575 (2009).
[26] I. G. Hughes and T. P. A. Hase, Measurements and their Uncertainties: A Practical Guide to Modern Error Analysis (Oxford University Press, Oxford, 2010).